Strain splitting of 1*s* yellow orthoexciton of epitaxial orthorhombic Cu_2O films on MgO [110]

Y. Sun, Kirill Rivkin, J. Chen, and J. B. Ketterson
Physics and Astronomy Department, Northwestern University, Evanston, Illinois 60201

P. Markworth and R. P. Chang
Material Science and Engineering Department, Northwestern University, Evanston, Illinois 60201
(Received 11 March 2002; published 23 December 2002)

We investigated the optical properties of epitaxial orthorhomic cuprous oxide films grown on MgO [110]. Absorption measurements show clear excitonic peaks up to $n=5p$. Photoluminescence at 2 K shows several sharp emission peaks in the vicinity of 610 nm associated with a splitting of various 1*s* orthoexciton energy levels. The evolution of the peaks with temperature indicates that three peaks at higher energy are due to direct recombination of 1*s* yellow orthoexcitons and three corresponding peaks at lower energy are their phonon replicas. The symmetry of each level is identified by the polarization properties of their photoluminescence emissions. The observed splitting of the energy levels is used to calculate the coherency strain based on an earlier-parametrized theory for the level splitting by Waters *et al.* based on the known symmetry of the electronic states. This predicted strain is compared with that determined by x-ray diffraction measurements of the measured lattice parameters.

DOI: 10.1103/PhysRevB.66.245315 PACS number(s): 71.35.Cc

I. INTRODUCTION

Cu_2O is the first semiconductor which showed a hydrogenic exciton absorption series.[1] Since then, its excitonic properties have been extensively studied in bulk material.[2] A hole in the highest (Γ_5^+) valence band and an electron in the lowest (Γ_6^+) conduction band form a 12-fold-degenerate complex of exciton states, which split into four-fold-degenerate yellow exciton and eight-fold-degenerate green exciton states due to spin-orbit coupling. Electron-hole exchange further splits the fourfold yellow excitons into triplet (orthoexciton) and singlet (paraexciton) states.[3–5] The three degenerate yellow orthoexciton states transform as xy, yz, and zx under the symmetry operations of the O_h group. Due to the fact that the conduction and valence bands have the same parity, the direct radiative recombination of orthoexcitons, denoted as X_o, is electric-dipole forbidden but quadrupole allowed, while the paraexciton is optical inactive to even higher order. The splitting of the exciton energy levels has been studied earlier in uniaxial-stressed bulk Cu_2O crystals with resonant-Raman-scattering spectroscopy. The yellow exciton series was observed to split into two or three lines for a stress applied along the (001) or (110) directions, respectively.[4–6] The energy levels were calculated using an effective Hamiltonian formalism. Deformation potential and spin-spin exchange terms were treated as perturbations.[4,5] In the simulation, an exchange energy and three deformation potentials were used as adjustable parameters. The strain was calculated from the applied stress using the known elastic constants.

Cu_2O films have been prepared by a number of groups.[7–13] MgO has usually been chosen as the substrate because of its close lattice match to that of Cu_2O (mismatch $\sim 1.4\%$).[8–10] However, single-crystal-like Cu_2O films worthy of optical studies of excitons were not realized. Bulk Cu_2O is known to have a structural instability with pressure,[14–16] and this may be relevant to film growth under stress. By subtly controlling the temperature and partial pressure near the solid-liquid transition, we earlier achieved the growth of high-quality epitaxial orthorhombic Cu_2O thin films on MgO[110] substrates.[17] In this paper, we report the excitonic structure observed in such epitaxial films. The splitting and shift of the 1s orthoexciton energy level were analyzed in terms of the distortion from the cubic structure of the bulk material.

II. SAMPLE PREPARATION AND CHARACTERIZATION

The Cu_2O films were prepared by the following procedures. Cu was first deposited under high vacuum on MgO substrates. These specimens were then placed in a quartz tube within which the oxygen pressure could be controlled and monitored; the tube was in turn located in a resistively heated furnace. The specimens were then heated and cooled according to various protocols described elsewhere.[17] The key requirement is that the sample be heated to a temperature at or slightly above the melting temperature but not so high as to cause the film to ''bead up'' into islands. Under this condition smooth shiny, epitaxial Cu_2O films often resulted. This procedure could be classified as a variant of liquid-phase epitaxy.

Two films we investigated in the present work. Both films had shiny surfaces with an orange-purplish color. However, the Cu_2O film on sample A spread uniformly on the substrate, while for sample B was a 5 mm$\times$5 mm island which coalesced near the center of the 8 mm^2 MgO substrate. The difference between the two samples results from the extreme temperature sensitivity of the wetting properties near solid-liquid equilibrium line. Sample A was likely closer

TABLE I. Measured parameters and strain tensor elements.

(a) Parameters determined by x-ray diffraction	Bulk	Sample B	Sample A
220 ($d/2\theta$)	1.510 Å/61.344°	1.520 Å/60.890°	1.524 Å/60.727°
200 ($d/2\theta$)	2.135 Å/42.297°	2.140 Å/42.194°	2.144/42.115°
111 ($d/2\theta$)	2.146 Å/36.418°	2.473 Å/36.290°	2.473 Å/36.295°
ω_{220}	NA	0.13°	0.2°
(b) Strain tensor elements determined from (a)			
ε_{zz}	0	−0.0034	−0.0084
ε_{xx}	0	0.0031	0.0050
ε_{xy}	0	0.0045	0.0053

to the solid-liquid line, while the temperature for sample B is presumed to be slightly above this line.

A Kappa diffractometer and Rikagu 18 KW rotating anode x-ray generator were used for θ-2θ, ω, and ϕ scans. The $K\alpha_1$ line was selected by a SiC monochromator. The full width at half maximum (FWHM) of the rocking curve obtained from an ω scan is a measure of the mosaic spread. The angular peak position of the θ-2θ curves gives the lattice constants. We now describe the four-circle x-ray diffraction (XRD) measurements used to determine the principal lattice constants of the Cu_2O films grown on MgO (110). The θ-2θ scan gives the angular peak position for the (220) planes when $\chi=0$. Titling χ to 45° allows a measurement of the 2θ peak position to the (200) planes. Titling χ to 35.26° and rotating ϕ to 90° allows a measurement of the 2θ peak position for the (111) planes.

Using the 2θ peak positions of the MgO substrate as the calibration, we find that all the 2θ peak positions measured for our Cu_2O film were shifted to smaller values than those of a bulk crystal, which implies that the film expanded in a direction perpendicular to the substrate plane. Using Bragg's law with $\lambda = 1.540\,56$ Å and 2θ peak positions, we can calculate the d_{220}, d_{200}, and d_{111} spacing. Considering a base-centered orthorhombic structure, the strain tensor ϵ_{ij} can be extracted from the above d spacings. Table I(a) lists the peak angles, d spacings, and rocking curve widths extracted from a scan in the (220) plane. Table I(b) lists the strain tensor elements calculated from the data of Table I(a).

III. OPTICAL MEASUREMENTS

A. Instrumentation

To characterize the optical properties of the films, we measured the transmission and photoluminescence spectra of samples A and B. Absorption measurements on Cu_2O films on MgO at room temperature were carried out using a Cary 1E UV/Vis Spectrometer. For absorption and photoluminescence spectra at low temperatures, the sample was loaded in the sample space of a Janis-variable-gas-flow cryostat. For the absorption setup, incandescent light was passed through several pinholes to reduce the beam size to around 2 mm; this beam was incident normal to the film. A set of neutral-density filters were placed between the pinhole and cryostat optical windows; the purpose was to improve the signal-to-noise ratio by integrating the signal for a longer time without simultaneously saturating the charge-coupled device (CCD).

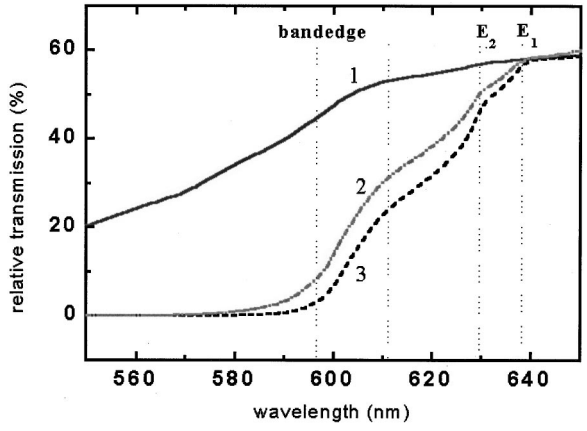

FIG. 1. Room-temperature transmission spectra of Cu_2O. Line 1 is for a single 2.5-μm Cu_2O thin film. Line 2 is for a stack of five 2.5-μm Cu_2O films. Line 3 is for a thin slab of natural Cu_2O single crystal.

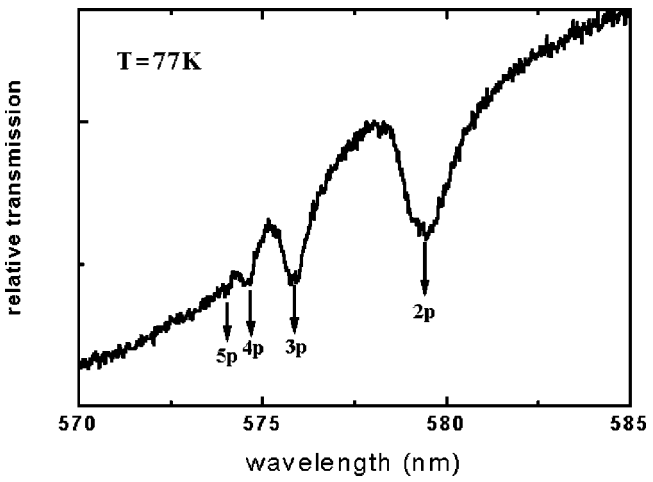

FIG. 2. Transmission spectra of a 2.5-μm Cu_2O thin film at 77 K; the $n=2,3,4,5$ exciton absorption peaks are marked.

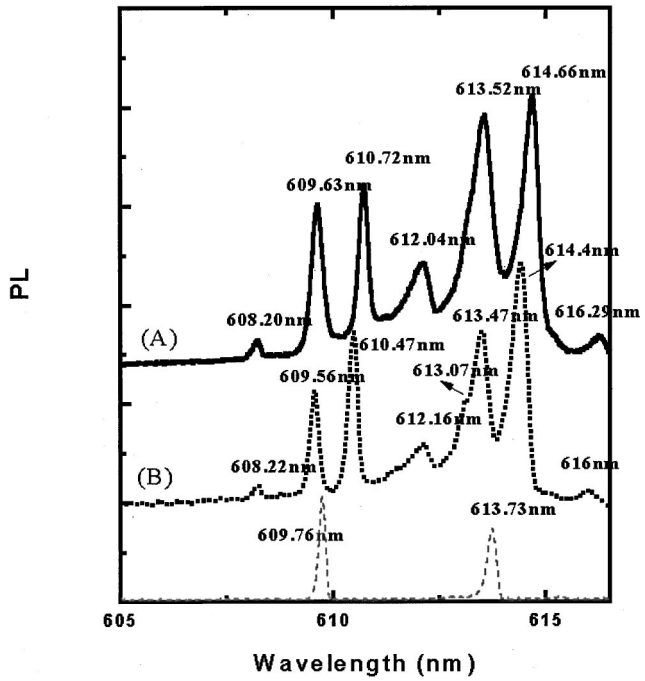

FIG. 3. Photoluminescence spectra of a Cu_2O film on MgO (110) at 2 K. Line (A) is for sample A, and line (B) is for sample B. The dotted line at the bottom is from natural bulk crystal.

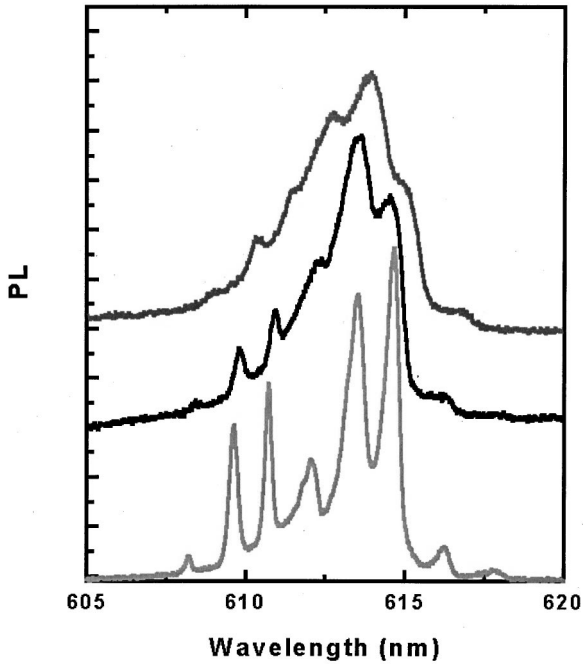

FIG. 4. Photoluminescence spectra from a Cu_2O film for different temperatures: 2 K, 18 K, and 30 K, from bottom to top, respectively.

The transmitted signal was collected by a lens combination which imaged the sample onto the input surface of a fiber-optic bundle. The signal was detected by SpecOne 500M spectrometer equipped with a liquid-nitrogen-cooled CCD. For the luminescence setup, the output beam of a CW 514.5 nm argon laser was filtered by a narrow-band pass filter (centered at 514.5 nm with bandwidth 10 nm). The laser beam was incident on the sample at an angle of 20° to the surface normal. The luminescence was collected by the lens combination from the direction normal to the film surface. An OG570 low-pass filter was placed after the lens to attenuate the pumping beam. To study the polarization properties of the photoluminescence, we placed a cube polarizer after the lens.

B. Measurements of the absorption spectrum

Absorption spectra were used to measure the band gap and principal-exciton series in our Cu_2O films. The absorption spectra are similar for the two samples. Figure 1 shows the absorption spectra taken at room temperature. Line 1 in Fig. 1 shows the room-temperature absorption spectrum from the 2.5-μm film on MgO (110). To identify the features in the spectrum, we compared the absorption spectrum from the 2.5-μm Cu_2O film with that from a thin (~ 10 μm) slab of high-quality natural Cu_2O single crystal; this is shown as line 3 in Fig. 1. To better show the detailed absorption features, a film was cut into identical pieces and the absorption spectrum was measured from a stack of five of them, as indicated by line 2. The absorption spectra of the film and the high-quality natural single crystal show similar features. The two features marked as E_1 and E_2 correspond to absorption transitions involving the absorption and emission of a Γ_{12}^- optical phonon,[1] respectively. The bandedge is around 595 nm. Other features may be due to (1) transitions of yellow 1s orthoexcitons involving other phonons and (2) transitions of 1s green excitons involving phonons. At 77 K, the absorption spectrum reveals four distinct exciton transitions ($n=2p$, $3p$, $4p$, $5p$), as shown in Fig. 2. The 1s (yellow) orthoexcitons cannot be seen in the absorption spectra since the film is too thin (this transition is only quadrupole allowed). We believe this is the first time that clean excitonic absorption lines have been observed in a heteroepitaxial Cu_2O film. Exciton peaks up to $n=12p$ have been previously reported on a high-quality thin natural bulk crystal.[18] We tested our system with a high quality natural crystal. It showed only the $n=2p-5p$ absorption peaks, which suggests that the number of exciton lines observed in the films may be limited by the resolution of our detection system.

C. Measurements of the emission spectra

Since the one-photon direct transition to the 1s orthoexciton is only quadrupole allowed, our films are too thin to show this feature in absorption. However, as noted above, the photoluminescence from the film shows clear 1s orthoexciton emission features. Figure 3 shows the photoluminescence spectra of the film at 2 K. The solid line is from sample A and the dotted line is from sample B. The dashed line at the bottom of the figure is from a natural single crystal. As the dashed line shows, the dominant spectral feature for a Cu_2O single crystal is the quadrupole direct recombination emission at 609.76 nm, denoted as X_o, and its Γ_{12}^- phonon replica at 613.73 nm. In these films, the orthoexciton degeneracy is totally lifted and it splits into three energy

TABLE II. Exciton parameters as determined from Raman measurements (Ref. 4).

Exciton (symmetry)	Wave function
Yellow paraexciton ($^1\Gamma_2^+$)	$\phi_{12}=\phi_{yn}\left(\frac{1}{\sqrt{12}}\right)[Y''(\alpha\beta_c+\beta\alpha_c)+2Y_2^{-1}\beta\beta_c-2Y_2^1\alpha\alpha_c]$
Yellow orthoexciton ($^3\Gamma_2^+$)	$\phi_5^{yz}=\phi_{yn}\left(\frac{-i}{\sqrt{12}}\right)[Y''(\alpha\alpha_c+\beta\beta_c)+2Y_2^{-1}\beta\alpha_c-2Y_2^1\alpha\beta_c]$
(electric quadrupole)	$\phi_8^{zx}=\phi_{yn}\left(\frac{1}{\sqrt{12}}\right)[Y''(-\alpha\alpha_c+\beta\beta_c)-2Y_2^{-1}\beta\alpha_c-2Y_2^1\alpha\beta_c]$
	$\phi_{10}^{xy}=\phi_{yn}\left(\frac{-i}{\sqrt{12}}\right)[Y''(\beta\alpha_c-\alpha\beta_c)-2Y_2^{-1}\beta\beta_c-2Y_2^1\alpha\alpha_c]$
Green exciton ($^3\Gamma_5^+$)	$\phi_3^x=\phi_{gn}\left(\frac{i}{\sqrt{8}}\right)[Y''(\alpha\alpha_c+\beta\beta_c)+2Y_2^1(\alpha\beta_c+\beta\alpha_c)-2Y_2^{-1}(\beta\alpha_c+\alpha\beta_c)]$
(magnetic dipole)	$\phi_6^y=\phi_{gn}\left(\frac{1}{\sqrt{8}}\right)[Y''(-\alpha\alpha_c+\beta\beta_c)+2Y_2^1(\alpha\beta_c+\beta\alpha_c)-2Y_2^{-1}(\beta\alpha_c+\alpha\beta_c)]$
	$\phi_1^z=\phi_{gn}\left(\frac{i}{\sqrt{2}}\right)(Y_2^{-1}\alpha\alpha_c-Y_2^1\beta\beta_c)$
Green exciton ($^2\Gamma_3^+$)	$\phi_2=\phi_{gn}\left(\frac{-1}{\sqrt{2}}\right)[Y_2^{-1}\alpha\alpha_c-Y_2^1\beta\beta_c)]$
(electric quadrupole)	$\phi_{11}=\phi_{gn}\left(\frac{-1}{\sqrt{6}}\right)[Y''(\beta\alpha_c+\alpha\beta_c)-Y_2^{-1}\beta\beta_c+Y_2^1\alpha\alpha_c]$
Green exciton ($^3\Gamma_5^+$)	$\phi_4^{yz}=\phi_{gn}\frac{-i}{\sqrt{24}}[Y''(\alpha\alpha_c+\beta\beta_c)+3(Y_2^{-1}\alpha\beta_c-Y_2^1\beta\varepsilon_c)+Y_2^{-1}\alpha\beta_c-Y_2^1\beta\alpha_c]$
(electric quadrupole)	$\phi_7^{zx}=\phi_{gn}\frac{1}{\sqrt{24}}[Y''(-\alpha\alpha_c+\beta\beta_c)-3(Y_2^{-1}\alpha\beta_c+Y_2^1\beta\varepsilon_c)+Y_2^{-1}\beta\alpha_c+Y_2^1\alpha\beta_c]$
	$\phi_9^{xy}=\phi_{gn}\frac{1}{\sqrt{6}}[Y''(\beta\alpha_c-\alpha\beta_c)+Y_2^1\alpha\alpha_c+Y_2^{-1}\beta\beta_c]$

levels. The three peaks at higher energy are the direct recombination lines. The three peaks at lower energy, and adjacent to them, are their Γ_{12}^- phonon replicas. We identified the emission features based on two observations. First, the photon energy differences between the 1-4, 2-5, and 3-6 peaks are the same and equal to the energy of bulk Γ_{12}^-phonons ($\sim$13 meV); second, as we increase the temperature, the intensity of the three peaks at higher energy decreases while the peaks at lower energy broaden and their intensity increases, as shown in Fig. 4. A similar phenomenon is observed in natural crystals. Since less excitons occupy the low-kinetic-energy states at high temperatures, the intensity of the X_o emission decreases and eventually disappears. The broadening of the phonon-assisted emission features with increasing bath temperature suggests that the excitonic temperature is in equilibrium with the bath temperature. The small peak at 616.26 nm (616 nm) for sample A (B) is the Γ_{15}^- phonon-assisted emission of the lowest orthoexciton energy level. We note slight differences in the peak positions for X_o emission and their associated phonon-assisted emission between the two samples. This is not surprising when we consider the different lattice parameters for the two samples. We will discuss this energy splitting in Sec. IV. The linewidths of the three X_o emissions are $\sim$0.4 nm for sample A and $\sim$0.27 nm for sample B, while the linewidth of X_o emission for a natural crystal under the same experimental conditions is $\sim$0.15 nm, which is the limit of our resolution. The broadening of the X_o emission peaks might arise from two causes: (1) a distribution of lattice constants, as characterized by the half width of the rocking curve, and (2) a shortening of the exciton lifetime resulting from defects in the sample. Sample B has a smaller rocking curve FWHM (0.13°) than that of sample A (0.2°); it also has a sharper X_o emission peak than that of sample A, which indicates that strain inhomogenity is an important mechanism in broadening the X_o emission peak. Since we do not have time-

resolved data on orthoexciton photoluminescence (PL) for these films, it is not clear how seriously the defects affect the orthoexciton lifetime.

The polarization properties of each PL peak were studied to identify their symmetry. The symmetry of an orthorhombic Bravis lattice is D_{2h}. The Γ_{25}^{+} O_h orthoexcitons split into Γ_3^+, Γ_4^+, and Γ_1^+ orthoexcitons. The basis functions for Γ_3^+, Γ_4^+, and Γ_1^+ are $z(x-y)$, $z(x+y)$, and xy.[19] Using the quadrupole operator to analyze the X_o emission, we see that direct emission from the Γ_3^+ state is not allowed. The Γ_4^+ state is linearly polarized along the [001] direction, while Γ_1^+ is linearly polarized along the $[1\bar{1}0]$. Our experimental result is that peak 2 is partially linearly polarized along [001], peak 3 is partially linearly polarized along $[1\bar{1}0]$, and peak 1 is much weaker than peaks 2 and 3. This indicates that peak 1 is a Γ_3^+ state, peak 2 is a Γ_4^+ state, and peak 3 is a Γ_1^+ state. The weak signal for peak 1 and the partially linear polarization of the remaining two can be the result of scattering and light collection in a cone along the [110] direction which causes a deviation of the experimental results from the ideal predictions of the theory. Using the dipole operator to analyze the Γ_{12}^{-} phonon-assisted emissions, we see that the Γ_3^+ state is linearly polarized along [001], Γ_4^+ is linearly polarized along $[1\bar{1}0]$, and Γ_1^+ is linearly polarized along $[1\bar{1}0]$. Experimentally we find that peak 4 is partially linearly polarized along [001], peak 5 is partially linearly polarized along $[1\bar{1}0]$, and peak 6 is partially linearly polarized along $[1\bar{1}0]$.

Due to the reduced symmetry in the films, direct recombination of paraexcitons should be allowed, theoretically. A close examination of peak 5 for sample A shows a small kink on the left wing, which is more pronounced for sample B (at 613.07 nm). It may be due to paraexciton direct recombination.

IV. PARAMETRIZATION OF THE ORTHOEXCITON EMISSION DATA

We now use the effective Hamiltonian formalism to analyze the energy splitting of X_o emission of the films. The 12 exciton basis functions from Refs. 4 and 5 are listed in Table II. To block diagonalize the effective Hamiltonian matrix, we used a different 12-exciton basis set given in Table III, which takes into account the different symmetries of the excitons in the orthorhombic structure. The effective Hamiltonian is block diagonalized into four 3×3 blocks, the elements of which are given in Table IV. The three orthoexcitons (ψ_5, ψ_8, ψ_{10}) and paraexciton (ψ_{12}) appear in separate blocks, which allows us to accurately solve for the eigenvalues. The parameters characterizing the exciton splitting were taken from Refs. 4 and 5 and are listed in Table V.

It is important to emphasize the strain tensor elements that we derived from our x-ray diffraction studies apply only to room temperature, whereas our measurements of the splitting of the X_0 line were carried out at helium temperatures. Clearly one must be concerned about the effect of differential thermal contraction. The direct approach would be to measure the lattice constants at helium temperatures; however, a cryogenic diffractometer was not locally set up. Furthermore, the unusual behavior of Cu_2O reported in Refs. 14–16, and the fact that the strain does not relax in our rather thick films (which led us to earlier conjecture the possible presence of a metastable structure for strongly strained Cu_2O; see Ref. 17) suggest that a simple estimate of the effect of differential contraction is not unreliable.

TABLE III. Exciton wave functions for a base-centered orthorhombic Cu_2O film on MgO(110).

$$\psi_1=-\phi_1$$
$$\psi_2=\phi_2$$
$$\psi_3=\frac{1}{\sqrt{2}}(\phi_2+\phi_6)$$
$$\psi_4=\frac{-1}{\sqrt{2}}(\phi_4+\phi_7)$$
$$\psi_5=\frac{-1}{\sqrt{2}}(\phi_5+\phi_8)$$
$$\psi_6=\frac{1}{\sqrt{2}}(\phi_3-\phi_6)$$
$$\psi_7=\frac{1}{\sqrt{2}}(\phi_4-\phi_7)$$
$$\psi_8=\frac{1}{\sqrt{2}}(\phi_5-\phi_8)$$
$$\psi_9=\phi_9$$
$$\psi_{10}=\phi_{10}$$
$$\psi_{11}=\phi_{11}$$
$$\psi_{12}=\phi_{12}$$

In the earlier Raman studies the strains were obtained more or less directly from the applied stress and the known elastic constants. We therefore elected to use the *earlier measured parameters* characterizing the effects of strain on the exciton spectra (reported by Waters *et al.*[4,5] and given in Table V) and our *measured splitting* of the exciton lines to *calculate the strain* present in our film. The overall consistency is then judged by a comparison of the *calculated low temperature strains* with our *measured room temperature strains*, as listed in Table I. The fitted and measured energy shifts of orthoexcitons for samples A and B and the predicted strains are listed in Table VI. The agreement between the low-temperature predicted and the room-temperature measured strains for sample A is rather good, given the above-stated reservations. The agreement for sample B is more qualitative. However, given our earlier discussion, in which it was emphasized that the overall quality of sample A was superior to sample B, we judge these results reasonable.

TABLE IV. Effective Hamiltonian matrix.

	ψ_2	ψ_9	ψ_{10}
ψ_2	$\Delta+E_c^g+\frac{1}{2}J_g+aTr\varepsilon$ $-3b(\varepsilon_{xx}-\varepsilon_{zz})$	$-6d\varepsilon_{xy}$	$-6d\sqrt{2}\varepsilon_{xy}$
ψ_9	$-6d\varepsilon_{xy}$	$\Delta+E_c^g-\frac{5}{6}J_g+aTr\varepsilon$ $-3b(\varepsilon_{xx}-\varepsilon_{zz})$	$\frac{4}{3\sqrt{2}}J-3\sqrt{2}b(\varepsilon_{xx}-\varepsilon_{zz})$
ψ_{10}	$-6d\sqrt{2}\varepsilon_{xy}$	$\frac{4}{3\sqrt{2}}J-3\sqrt{2}b(\varepsilon_{xx}-\varepsilon_{zz})$	$E_c^y-\frac{1}{6}J_y+aTr\varepsilon$
	ψ_2	ψ_9	ψ_{10}
ψ_1	$\Delta+E_c^g+\frac{1}{2}J_g+aTr\varepsilon$ $-3b(\varepsilon_{xx}-\varepsilon_{zz})$	$-6d\varepsilon_{xy}$	$-6d\sqrt{2}\varepsilon_{xy}$
ψ_{11}	$-6d\varepsilon_{xy}$	$\Delta+E_c^g+\frac{1}{2}J_g+aTr\varepsilon$ $-3b(\varepsilon_{xx}-\varepsilon_{zz})$	$-3\sqrt{2}b(\varepsilon_{xx}-\varepsilon_{zz})$
ψ_{12}	$-6d\sqrt{2}\varepsilon_{xy}$	$-3\sqrt{2}b(\varepsilon_{xx}-\varepsilon_{zz})$	$E_c^y+\frac{1}{2}J_y+aTr\varepsilon$
	ψ_4	ψ_5	ψ_6
ψ_4	$\Delta+E_c^g-\frac{5}{6}J_g+a\mathrm{Tr}\varepsilon$ $+3\sqrt{3}d\varepsilon_{xy}-\frac{3}{2}b(\varepsilon_{xx}-\varepsilon_{zz})$	$\frac{4}{3\sqrt{2}}J-3\sqrt{6}d\varepsilon_{xy}$ $+\frac{3}{\sqrt{2}}b(\varepsilon_{xx}-\varepsilon_{zz})$	$\frac{3\sqrt{3}}{2}b(\varepsilon_{xx}-\varepsilon_{zz})$ $+3d\varepsilon_{xy}$
ψ_5	$\frac{4}{3\sqrt{2}}J-3\sqrt{6}d\varepsilon_{xy}$ $+\frac{3}{\sqrt{2}}b(\varepsilon_{xx}-\varepsilon_{zz})$	$E_c^y-\frac{1}{6}J_y+a\mathrm{Tr}\varepsilon$	$3\sqrt{\frac{3}{2}}b(\varepsilon_{xx}-\varepsilon_{zz})$ $+3\sqrt{2}d\varepsilon_{xy}$
ψ_6	$\frac{3\sqrt{3}}{2}b(\varepsilon_{xx}-\varepsilon_{zz})$ $+3d\varepsilon_{xy}$	$3\sqrt{\frac{3}{2}}b(\varepsilon_{xx}-\varepsilon_{zz})$ $+3\sqrt{2}d\varepsilon_{xy}$	$\Delta+E_c^g+\frac{1}{2}J_g+a\mathrm{Tr}\varepsilon$ $-3\sqrt{3}d\varepsilon_{xy}+\frac{3}{2}b(\varepsilon_{xx}-\varepsilon_{zz})$
	ψ_3	ψ_7	ψ_8
ψ_3	$\Delta+E_c^g-\frac{1}{2}J_g+a\mathrm{Tr}\varepsilon$ $+3\sqrt{3}d\varepsilon_{xy}+\frac{3}{2}b(\varepsilon_{xx}-\varepsilon_{zz})$	$-\frac{3\sqrt{3}}{2}b(\varepsilon_{xx}-\varepsilon_{zz})$ $+3d\varepsilon_{xy}$	$-3\sqrt{\frac{3}{2}}b(\varepsilon_{xx}-\varepsilon_{zz})$ $+3\sqrt{2}d\varepsilon_{xy}$
ψ_7	$-\frac{3\sqrt{3}}{2}b(\varepsilon_{xx}-\varepsilon_{zz})$ $+3d\varepsilon_{xy}$	$\Delta+E_c^g-\frac{5}{6}J_g+a\mathrm{Tr}\varepsilon$ $-3\sqrt{3}d\varepsilon_{xy}-\frac{3}{2}b(\varepsilon_{xx}-\varepsilon_{zz})$	$\frac{4}{3\sqrt{2}}J+3\sqrt{6}d\varepsilon_{xy}$ $+\frac{3}{\sqrt{2}}b(\varepsilon_{xx}-\varepsilon_{zz})$
ψ_8	$-3\sqrt{\frac{3}{2}}b(\varepsilon_{xx}-\varepsilon_{zz})$ $+3\sqrt{2}d\varepsilon_{xy}$	$\frac{4}{3\sqrt{2}}J+3\sqrt{6}d\varepsilon_{xy}$ $+\frac{3}{\sqrt{2}}b(\varepsilon_{xx}-\varepsilon_{zz})$	$E_c^y-\frac{1}{6}J_y+a\mathrm{Tr}\varepsilon$

TABLE V. Measured electron splitting parameters.

Exciton parameters as from Raman (Ref. 4)	determined measurements
J	$-183\ \mathrm{cm}^{-1}$
J_y	$J/2$
J_g	$2J$
Δ	$600\ \mathrm{cm}^{-1}$
a	-1.8 eV
b	-0.3 eV
d	0.5 eV
E_g	$(18588\text{-}1242)\ \mathrm{cm}^{-1}$
E_y	$(17523\text{-}795)\ \mathrm{cm}^{-1}$

V. CONCLUSIONS

In summary, we have investigated the excitonic properties of two epitaxial orthorhombic Cu_2O films grown on MgO (220). A clear exciton absorption series and an energy splitting of the 1s orthexciton emissions are observed. We note that coherent-exciton effects in Cu_2O, such as BEC, quadrupole polaritons, and exciton superfluid-soliton propagation, have only been investigated in natural bulk crystal.[20–22] When comparing a Cu_2O bulk crystal to Cu_2O films, we note several unique advantages for studying coherent excitonic effects: (1) films provide at least a one-dimensional confinement of the excitons, which should lead to higher exciton densities and a better estimate of that density; (2) films are in better thermal contact with the environment, which should lead to more rapid cooling following a pump pulse; (3) the strain induced by the lattice mismatch between the Cu_2O film and the MgO substrate can lift the degeneracy of the orthoexcitons states (resulting in a higher density in the lowest level) and, theoretically, might lead to the direct observation of the optically-forbidden paraexcitons; and (4) since lithographic patterning and etching of the films is relatively straightforward, high-quality patterned films with good optical properties could be used to perform a variety of exciting experiments, such as fabricating an exciton Josephson junction, confining an exciton condensate, propagating polaritons in a waveguide, etc.

ACKNOWLEDGMENTS

We would like to acknowledge useful discussions with Keith O'Hara on the theory. Help from Michael Bedzyk, Zhan Zhang, Brad Tinkham, and Duane Goodner in using the Kappa 18KW XRD facility is also acknowledged. This research was supported by the Northwestern Materials Research Center through National Science Foundation-MRSEC program under Grant No. DMR-9632472.

TABLE VI. Predicted energy splittings.

Energy	Measured value (eV)	Fitted value (eV)	Error (%)
Sample A: calculated $\varepsilon_{xx}=0.005$, $\varepsilon_{xy}=0.005299$, $\varepsilon_{zz}=-0.0084$			
E_{ground} orthoexitons	2.034	2.040925	0.34
Energy splittings:			
E_5	0.00037	0.00037	0.03
E_{10}	-0.00326	-0.000448	86.26
E_8	0.00515	0.004479	13.04
Sample B: calculated $\varepsilon_{xx}=0.004580$, $\varepsilon_{xy}=0.003488$, $\varepsilon_{zz}=-0.017$			
Energy	Measuredvalue(eV)	Fittedvalue(eV)	Error(%)
Energy splittings:			
E_5	0.0006	0.000583	2.76
E_{10}	-0.00243	-0.002611	7.47
E_8	0.00508	0.00669	31.69

Fitting parameters: $a=0.05$, $b=0.32004$, $d=0.4876$, $\Delta=0.094$ eV, $J=-0.0227$ eV.

[1] P.W. Baumeister, Phys. Rev. **121**, 359 (1961).
[2] V.T. Agekyan, Phys. Status Solidi A **43**, 11 (1977).
[3] R.J. Elliott, Phys. Rev. **124**, 340 (1961).
[4] R.G. Waters, Fred H. Pollak, R.H. Bruce, and H.Z. Cummins, Phys. Rev. B **21**, 1665 (1980).
[5] R. G. Waters, Ph.D. thesis, City University of New York, 1979.
[6] H.R. Trebin, H.Z. Cummins, and J.L. Birman, Phys. Rev. B **23**, 597 (1981).
[7] A. Parretta, M.K. Jayaraj, A.D. Nocera, S. Loreti, L. Quercia, and A. Agati, Phys. Status Solidi A **155**, 399 (1996).
[8] D.J. Miller, J.D. Hettinger, R.P. Chiarello, and H.K. Kim, J. Mater. Res. **7**, 2828 (1992).
[9] S.B. Ogale, P.G. Bilurkar, N. Mate, S.M. Kanetkar, N. Parikh, and B. Patnaik, J. Appl. Phys. **72**, 765 (1992).
[10] S.B Ogale, P.G. Bilurkar, and N. Mate, J. Cryst. Growth **128**, 714 (1993).

[11] M.W. Bench, K.B. Sartain, J.R. Heffelfinger, and C.B. Carter, in *Mechanisms of Thin Film Evolution*, edited by S.M. Yalisove, C.V. Thompson, and D.J. Eaglesham, Mater. Res. Soc. Symp. Proc. **317** (Materials Reasearch Society, Pittsburgh, 1974), p. 491.
[12] M. Ottosson, J. Lu, and J-O. Carlsson, J. Cryst. Growth **151**, 305 (1995).
[13] K. Kawaguchi, R. Kita, M. Nishiyama, and T. Morishita, J. Cryst. Growth **143**, 221 (1994).
[14] M.H. Manghnani, W.S. Brower, and H.S. Parker, Phys. Status Solidi A **25**, 69 (1974).
[15] G.K. White, J. Phys. C **11**, 2171 (1978).
[16] A. Werner and H.D. Hochheimer, Phys. Rev. B **25**, 5929 (1982).
[17] P.R. Markworth, R.P.H. Chang, Y. Sun, G.K.L. Wong, and J.B. Ketterson, J. Mater. Res. **16**, 914 (2001).
[18] H. Mstsumoto *et al.*, Solid State Commun. **97**, 125 (1996).
[19] G.F. Koster, J.O. Dimmock, R. G. Wheeler, and H. Statz, *Properties of the Thirty-Two Point Groups* (MIT Press, Cambridge, MA, 1963).
[20] Jia Ling Lin and J.P. Wolfe, Phys. Rev. Lett. **71**, 1222 (1993).
[21] D. Frohlich, A. Kulik, B. Uebbing, A. Mysyrowicz, V. Langer, H. Stolz, and W. von der Oster, Phys. Rev. Lett. **67**, 2343 (1991).
[22] E. Fortin, S. Farad, and A. Mysyrowicz, Phys. Rev. Lett. **70**, 3951 (1993).